# Computing Volume Bounds of Inclusions by Eit Measurements

**Giovanni Alessandrini · Antonio Bilotta ·
Antonino Morassi · Edi Rosset · Emilio Turco**

**Abstract** The size estimates approach for Electrical Impedance Tomography (EIT) allows for estimating the size (area or volume) of an unknown inclusion in an electrical conductor by means of one pair of boundary measurements of voltage and current. In this paper we show by numerical simulations how to obtain such bounds for practical application of the method. The computations are carried out both in a 2-D and a 3-D setting.

## 1 Introduction

EIT is aimed at imaging the internal conductivity of a body from current and voltage measurements taken at the boundary. It is well known [1, 2], that, even in the ideal situation in which all possible boundary measurements are available, the correspondence *boundary data → conductivity* is highly (exponentially) unstable. As a consequence it is evident that, in practice, it is impossible to distinguish high resolution features of the interior from limited and noisy boundary data [3].

Motivated by applications, a line of investigation pursued by many authors [4–11], has been the one of limiting the analysis to cases in which one seeks an unknown interior inclusion embedded in an otherwise known (may be even homogeneous) conductor, and whose conductivity is assumed to differ from the background.

G. Alessandrini · E. Rosset
Dipartimento di Matematica e Informatica, Università degli Studi di Trieste, Trieste, Italy

A. Bilotta
Dipartimento di Strutture, Università della Calabria, Rende (CS), Italy

A. Morassi
Dipartimento di Georisorse e Territorio, Università degli Studi di Udine, Udine, Italy

E. Turco (✉)
Dipartimento di Architettura e Pianificazione, Università degli Studi di Sassari, Alghero, Italy
e-mail: emilio.turco@uniss.it

Even in this restricted case, and even when full boundary data are available, the instability remains of exponential type [12].

It is therefore reasonable to further restrict the goal and attempt to evaluate some parameters expressing the size (area, volume) of the inclusion, disregarding its precise location and shape, having at our disposal one pair of boundary measurements of voltage and current. This approach, which can be traced back to [4], has been well developed theoretically [13–16], see also [17] and [18] for the analogous treatment in the linear elasticity framework. In order to describe such type of results we need first to introduce some notation.

We denote by $\Omega$ a bounded domain in $\mathbb{R}^n$, $n = 2, 3$, representing an electrical conductor. The boundary $\partial\Omega$ of $\Omega$ is assumed of Lipschitz class, with constants $r_0$, $M_0$, that is the boundary can be locally represented as a graph of a Lipschitz continuous function with Lipschitz constant $M_0$ in some ball of radius $r_0$. When no inclusion is present in the conductor we assume that it is homogeneous and, more specifically, we assume its conductivity $\sigma(x) \equiv 1$. When the conductor contains an unknown inclusion $D$ of different conductivity, say $k > 0$, $k \neq 1$ the overall conductivity in the conductor will be given by $\sigma(x) = 1 + (k-1)\chi_D(x)$. Here and in what follows it is assumed that $D$ is strictly contained in $\Omega$. More precisely, for a given $d_0 > 0$,

$$\text{dist}(D, \partial\Omega) \geq d_0. \tag{1.1}$$

Let $\varphi \in H^{-\frac{1}{2}}(\partial\Omega)$, $\int_{\partial\Omega} \varphi = 0$, be an applied current density on $\partial\Omega$. The induced electrostatic potential $u \in H^1(\Omega)$ is the solution of the Neumann problem

$$\begin{cases} \text{div}\,((1 + (k-1)\chi_D)\nabla u) = 0, & \text{in } \Omega, \\ \nabla u \cdot \nu = \varphi, & \text{on } \partial\Omega, \end{cases} \tag{1.2}$$

where $\nu$ denotes the outer unit normal to $\partial\Omega$.

When $D$ is the empty set, that is when the inclusion is absent, the reference electrostatic potential $u_0 \in H^1(\Omega)$ satisfies the Neumann problem

$$\begin{cases} \Delta u_0 = 0, & \text{in } \Omega, \\ \nabla u_0 \cdot \nu = \varphi, & \text{on } \partial\Omega. \end{cases} \tag{1.3}$$

In both cases (1.2) and (1.3), the solutions $u$ and $u_0$ are determined up to an additive constant.

Let us denote by $W$, $W_0$ the powers required to maintain the current density $\varphi$ on $\partial\Omega$ when $D$ is present or it is absent, respectively. Namely

$$W = \int_{\partial\Omega} u\varphi = \int_{\Omega} (1 + (k-1)\chi_D)|\nabla u|^2, \tag{1.4}$$

$$W_0 = \int_{\partial\Omega} u_0\varphi = \int_{\Omega} |\nabla u_0|^2. \tag{1.5}$$

The size estimate approach developed in [13–16], tells us that the measure $|D|$ of $D$ can be bounded from above and below in terms of the quantity $|\frac{W_0-W}{W_0}|$ which we call the normalized power gap. More precisely the following bounds hold, see [16, Theorem 2.3].

**Theorem 1.1** *Let $D$ be any measurable subset of $\Omega$ satisfying* (1.1). *Under the above assumptions, if $k > 1$ we have*

$$\frac{1}{k-1}C_1^+ \frac{W_0 - W}{W_0} \leq |D| \leq \left(\frac{k}{k-1}\right)^{\frac{1}{p}} C_2^+ \left(\frac{W_0 - W}{W_0}\right)^{\frac{1}{p}}. \tag{1.6}$$

*If, conversely, $k < 1$, then we have*

$$\frac{k}{1-k} C_1^- \frac{W - W_0}{W_0} \leq |D| \leq \left(\frac{1}{1-k}\right)^{\frac{1}{p}} C_2^- \left(\frac{W - W_0}{W_0}\right)^{\frac{1}{p}}, \tag{1.7}$$

*where $C_1^+$, $C_1^-$ only depend on $d_0$, $|\Omega|$, $r_0$, $M_0$, whereas $p > 1$, $C_2^+$, $C_2^-$ only depend on the same quantities and, in addition, on the frequency of $\varphi$*

$$F[\varphi] = \frac{\|\varphi\|_{H^{-\frac{1}{2}}(\partial\Omega)}}{\|\varphi\|_{H^{-1}(\partial\Omega)}}. \tag{1.8}$$

When it is a priori known that the inclusion $D$ is not too small (if it is at all present), a situation which often occurs in practical applications, stronger bounds apply.

**Theorem 1.2** *Under the above hypotheses, let us assume, in addition, that*

$$|D| \geq m_0, \tag{1.9}$$

*for a given positive constant $m_0$. If $k > 1$ we have*

$$\frac{1}{k-1} C_1^+ \frac{W_0 - W}{W_0} \leq |D| \leq \frac{k}{k-1} C_2^+ \frac{W_0 - W}{W_0}. \tag{1.10}$$

*If, conversely, $k < 1$, then we have*

$$\frac{k}{1-k} C_1^- \frac{W - W_0}{W_0} \leq |D| \leq \frac{1}{1-k} C_2^- \frac{W - W_0}{W_0}, \tag{1.11}$$

*where $C_1^+$, $C_1^-$ only depend on $d_0$, $|\Omega|$, $r_0$, $M_0$, whereas $C_2^+$, $C_2^-$ only depend on the same quantities and, in addition, on $m_0$ and $F[\varphi]$.*

Theorem 1.2 can be easily deduced from Theorem 1.1 by the arguments sketched in [19, Appendix].

One of the goals of the present paper is to test the applicability of such bounds by numerical simulations with the following purposes:

 (i) Provide practical evaluations of the constants $C_1^{\pm}$, $C_2^{\pm}$ appearing in the above inequalities (1.6), (1.7), (1.10), (1.11).
 (ii) When, due to special geometric configurations, we can solve (1.3) in closed form and it is possible to explicitly evaluate such constants, compare such theoretical values with those obtained by simulations.
(iii) Show that such upper and lower bounds deteriorate as the frequency $F[\varphi]$ increases.

The other goal of this paper is to perform similar kinds of numerical simulations when the so-called *complete model* of EIT is adopted. We recall that this model is aimed at an accurate description of the boundary measurements suitable for medical applications, and was introduced in [20] and subsequently developed in [21] and [22]. In this model, the metal electrodes behave as perfect conductors and provide a low-resistance path for current. An electrochemical effect at the contact between the electrodes and the body results in a thin, highly resistive, layer. The impedance of this layer is characterized by a positive quantity $z_l$ on each electrode $e_l$, $l = 1, \ldots, L$, which is called *surface impedance*.

Denoting by $I_l$ the current applied to each $e_l$, the resulting boundary condition on each electrode $e_l$ becomes

$$u + z_l \nabla u \cdot v = U^l, \quad \text{on } e_l, \tag{1.12}$$

where the unknown constant $U^l$ is the voltage which can be measured at the electrode $e_l$.

We assume, as before, that the reference conductor has conductivity $\sigma \equiv 1$ and that an unknown inclusion $D$ of conductivity $\sigma \equiv k$, with $k > 0$ and $k \neq 1$, is strictly contained in $\Omega$. Therefore, the electrostatic potential $u$ inside the conductor is determined, up to an additive constant, as the solution to the following problem

$$\begin{cases} \text{div}((1 + (k-1)\chi_D)\nabla u) = 0, & \text{in } \Omega, \\ u + z_l \nabla u \cdot v = U^l, & \text{on } e_l, 1 \leq l \leq L, \\ \nabla u \cdot v = 0, & \text{on } \partial\Omega \setminus \bigcup_{l=1}^{L} e_l, \\ \int_{e_l} \nabla u \cdot v = I_l, & 1 \leq l \leq L, \end{cases} \tag{1.13}$$

where the so-called current pattern $I = (I_1, \ldots, I_L)$ is subject to the conservation of charge condition $\sum_{l=1}^{L} I_l = 0$, and the unknown constants $U^l$ are the components of the so-called voltage pattern $U = (U^1, \ldots, U^L)$.

When the inclusion is absent, the electrostatic potential $u_0$ induced by the same current pattern $I$ is determined, up to an additive constant, as the solution of the following problem

$$\begin{cases} \Delta u_0 = 0, & \text{in } \Omega, \\ u_0 + z_l \nabla u_0 \cdot v = U_0^l, & \text{on } e_l, 1 \leq l \leq L, \\ \nabla u_0 \cdot v = 0, & \text{on } \partial\Omega \setminus \bigcup_{l=1}^{L} e_l, \\ \int_{e_l} \nabla u_0 \cdot v = I_l, & 1 \leq l \leq L, \end{cases} \tag{1.14}$$

where, as before, the $U_0^l$ are unknown constants in the direct problem (1.14).

We shall assume that the sets $e_1, \ldots, e_L$, representing the electrodes, are open, pairwise disjoint, connected subsets of $\partial\Omega$ and, in addition,

$$\text{dist}(e_l, e_k) \geq \delta_1 > 0 \quad \text{for every } l, k, l \neq k. \tag{1.15}$$

The surface impedance $z_l$ on $e_l$, $l = 1, \ldots, L$, is assumed to be real valued and to satisfy the following bounds

$$0 < m \leq z_l \leq M, \quad \text{for every } l = 1, \ldots, L. \tag{1.16}$$

In this formulation, the powers $W$ and $W_0$ become

$$W = \sum_{i=1}^{L} I_i U^i, \tag{1.17}$$

$$W_0 = \sum_{i=1}^{L} I_i U_0^i. \tag{1.18}$$

Size estimates like those of Theorems 1.1, 1.2 were obtained for the complete model in [23]. In particular we have

**Theorem 1.3** *Let $D$ be any measurable subset of $\Omega$ satisfying* (1.1) *and let $W$, $W_0$ be given by* (1.17), (1.18). *Then, inequalities* (1.6), (1.7) *hold for $k > 1$ and $k < 1$, respectively, where the constants $C_1^+$, $C_1^-$ only depend on $d_0$, $|\Omega|$, $r_0$, $M_0$, and $C_2^+$, $C_2^-$ and $p > 1$ only depend on the same quantities and, in addition, on $\delta_1$, $M$ and $m$.*

Also in this case, the size estimates of $|D|$ can be improved to the form (1.10), (1.11) when condition (1.9) is satisfied.

In Sect. 2 we consider the standard EIT setting. We start by describing the finite element setup used in our numerical simulations in Sect. 2.1. Next (as a warm-up) we consider a two-dimensional model in Sect. 2.2.

In Sect. 2.3 we consider the three-dimensional case and we discuss all items (i), (ii), (iii) introduced above. In particular we observe that, comparing the results as the frequency $F[\varphi]$ increases, we have quite rapidly a serious deterioration of the bounds. This poses a severe warning on the limitations that have to be taken into account in the choice of the boundary current profile $\varphi$.

Section 3 is devoted to simulations with the complete EIT model. In this case it is reasonable analyze the case when only two electrodes, one positive and one negative, are attached to the surface of the conductor. In this case, the frequency function is not available from the data since we are not prescribing the boundary current $\nabla u \cdot \nu_{|\partial\Omega}$ but only the current pattern, which is a 2-electrode configuration, is just the pair $(1, -1)$. In place of the frequency function, the parameters that may influence the constants in the volume bounds are: the width of the electrodes and the distance between them. We perform various experiments to test such variability.

## 2 Numerical Simulations for the EIT Model

### 2.1 Numerical Model

The numerical model is based on the discretization of the energy functional $J : H^1(\Omega, \mathbb{R}^n) \to \mathbb{R}$

$$J(u) = \frac{1}{2}\int_\Omega (1 + (k-1)\chi_D)\nabla u \cdot \nabla u - \int_{\partial\Omega} \varphi u, \tag{2.1}$$

associated with the variational formulation of problem (1.2). The energy functional (2.1) has been discretized by using the High Continuity (HC) technique already presented in [24] and [25] in the context of linear elasticity. Accordingly, for 2–D problems the electric potential on the $e$th finite element can be represented as

$$u_e = \sum_{i,j=1}^3 \phi_i(\xi_1)\phi_j(\xi_2)u_{ij}, \tag{2.2}$$

whereas for the 3-D case it assumes the form

$$u_e = \sum_{i,j,l=1}^3 \phi_i(\xi_1)\phi_j(\xi_2)\phi_l(\xi_3)u_{ijl}, \tag{2.3}$$
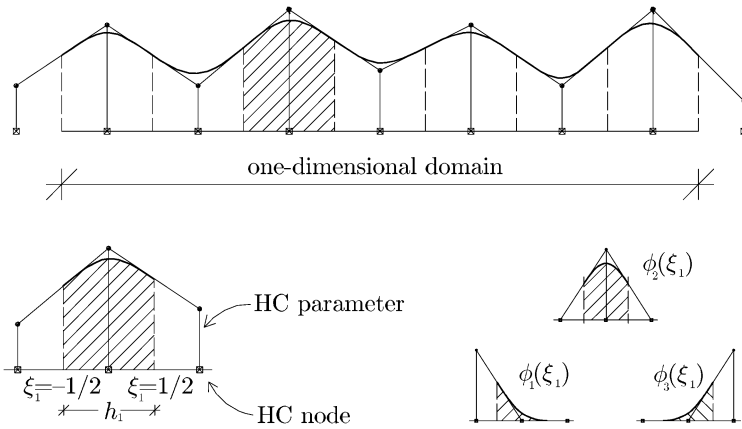
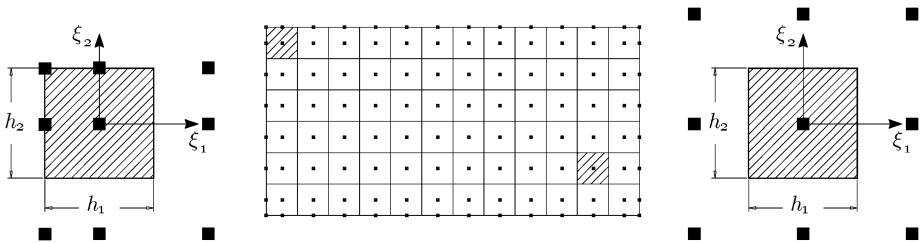**Fig. 1** HC interpolation in the 1-D case: nodes, parameters and shape functions



**Fig. 2** HC mesh in the 2-D case: nodes for boundary and inner elements

where the coordinates $\xi_r$, $r = 1, \ldots, n$, span the unitary element domain $[-\frac{1}{2}, \frac{1}{2}]^n$, $n = 2, 3$, and $u_{ij}$, $u_{ijl}$ are the HC parameters involved in the field interpolation on the generic element. The shape functions $\phi_i(\xi_r)$ are defined as

$$
\begin{cases}
\phi_1(\xi_r) = \dfrac{1}{8} - \dfrac{1}{2}\xi_r + \dfrac{1}{2}\xi_r^2, \\[2mm]
\phi_2(\xi_r) = \dfrac{3}{4} - \xi_r^2, \\[2mm]
\phi_3(\xi_r) = \dfrac{1}{8} + \dfrac{1}{2}\xi_r + \dfrac{1}{2}\xi_r^2.
\end{cases}
\tag{2.4}
$$

The 1-D case illustrated in Fig. 1 shows the meaning of the HC parameters. They allow us to define the slopes of the interpolated function at the end points of the element. On the same figure one can see also the positions of the HC nodes and the shape functions (2.4).

Figure 2 shows a typical structured mesh on a rectangular domain and the nodes used for the approximation of the potential field in the 2-D case. For elements with a side lying on the boundary, in order to easily impose the Neumann boundary conditions, special shape functions are used. In practice, the external HC nodes are translated onto the boundary $\partial\Omega$ and the related HC parameters have the meaning of function values (see again Fig. 2). In this case the shape functions relative to a *left* boundary ($\xi_r = -\frac{1}{2}$) and a *right* boundary ($\xi_r = \frac{1}{2}$)

of the finite element are

$$
\text{left :} \begin{cases} \phi_1(\xi_r) = \dfrac{1}{4} - \xi_r + \xi_r^2, \\[2mm] \phi_2(\xi_r) = \dfrac{5}{8} + \dfrac{1}{2}\xi_r - \dfrac{3}{2}\xi_r^2, \\[2mm] \phi_3(\xi_r) = \dfrac{1}{8} + \dfrac{1}{2}\xi_r + \dfrac{1}{2}\xi_r^2, \end{cases} \qquad \text{right :} \begin{cases} \phi_1(\xi_r) = \dfrac{1}{8} - \dfrac{1}{2}\xi_r + \dfrac{1}{2}\xi_r^2, \\[2mm] \phi_2(\xi_r) = \dfrac{5}{8} - \dfrac{1}{2}\xi_r - \dfrac{3}{2}\xi_r^2, \\[2mm] \phi_3(\xi_r) = \dfrac{1}{4} + \xi_r + \xi_r^2. \end{cases} \qquad (2.5)
$$

Further details about the HC interpolation can be found in [24] and [25]. This interpolation technique, which can be considered as a particular case of the Bézier interpolation, has the main advantage of reproducing potential fields of $C^1$ smoothness with a computational cost equivalent to a $C^0$ interpolation.

By (2.2) or (2.3), the potential field $u$ on each element $e$ takes the compact form

$$
u_e = \mathbf{N}_e \mathbf{w}_e. \qquad (2.6)
$$

The one-row matrix $\mathbf{N}_e$ collects the shape functions of the HC interpolation, whereas the components of the vector $\mathbf{w}_e$ are the nodal parameters of the underlying element. With this notation, the gradient of the potential field is given by

$$
\nabla u_e = \nabla \mathbf{N}_e \mathbf{w}_e. \qquad (2.7)
$$

We remark that the dimensions of the matrices $\mathbf{N}_e$, $\nabla \mathbf{N}_e$ and vector $\mathbf{w}_e$ are $1 \times 9$, $2 \times 9$ and $9 \times 1$ for the 2-D case and $1 \times 27$, $3 \times 27$ and $27 \times 1$ for the 3-D case.

By (2.6) and (2.7), the discrete form of (2.1) becomes

$$
J(\mathbf{w}_e) = \sum_e \left( \frac{1}{2} \int_{\Omega_e} (1 + (k-1)\chi_D)(\nabla \mathbf{N}_e \mathbf{w}_e) \cdot (\nabla \mathbf{N}_e \mathbf{w}_e) - \int_{\partial \Omega_e} \varphi \mathbf{N}_e \mathbf{w}_e \right), \qquad (2.8)
$$

or, in a compact form,

$$
J(\mathbf{w}_e) = \sum_e (\mathbf{w}_e^T \mathbf{K}_e \mathbf{w}_e - \mathbf{w}_e^T \mathbf{p}_e). \qquad (2.9)
$$

The latter equation provides the definition of the matrix and the vector associated with the $e$th element

$$
\begin{cases} \mathbf{K}_e = \int_{\Omega_e} (1 + (k-1)\chi_D)(\nabla \mathbf{N}_e)^T \nabla \mathbf{N}_e, \\[2mm] \mathbf{p}_e = \int_{\partial \Omega_e} \varphi \mathbf{N}_e, \end{cases} \qquad (2.10)
$$

which can be used to assemble, by using standard techniques, the system of equations to solve.

## 2.2 Two-Dimensional Case

Numerical analysis has been performed on a square conductor $\Omega$ of side $l$ under the two current density fields $\varphi$ illustrated in Fig. 3. The domain $\Omega$ has been discretized with a mesh of $21 \times 21$ HC finite elements and for both Test $T_1$ and Test $T_2$ of Fig. 3 we have considered an inclusion $D$ with conductivity $k = 0.1$ or $k = 10$.
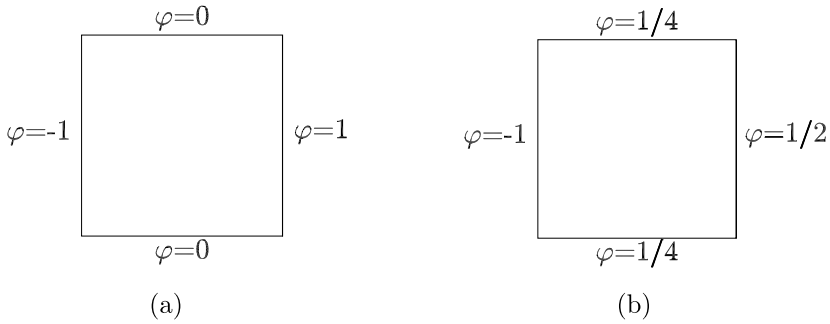
**Fig. 3** Square conductor considered in 2-D numerical simulations for the EIT model and applied current density fields: Test $T_1$ (**a**), Test $T_2$ (**b**)
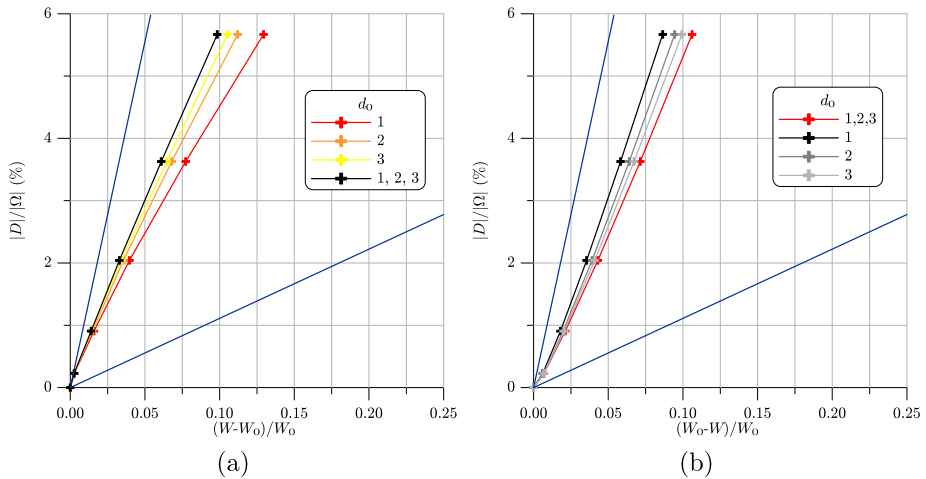


**Fig. 4** Influence of $d_0$ for square inclusions in Test $T_1$ of Fig. 3a ($21 \times 21$ FE mesh): $k = 0.1$ (**a**), $k = 10$ (**b**)

A first series of experiments has been carried out by considering all possible square inclusions with side ranging from 1 to 5 elements, that is the size of inclusion has been kept lower than 6% of the total size of the conductor. The results are collected in Figs. 4 and 5 for different values of the minimum distance $d_0$ between the inclusion $D$ and the boundary of $\Omega$.

From Figs. 4a and 5a, which refer to the case $k = 0.1$, one can note that the upper bound of $|D|$ is rather insensitive to the choice of $d_0$, whereas the lower bound in (1.11) improves as $d_0$ increases. The converse situation occurs when the inclusion is made by material of higher conductivity, see Figs. 4b and 5b.

As a second class of experiments, we have considered inclusions of general shape on a FE mesh of $15 \times 15$ HC elements. More precisely, each inclusion is the union of elements having at least a common side and being at least $d_0 = 2$ elements far from the boundary $\partial\Omega$. Results are collected in Figs. 6 and 7.
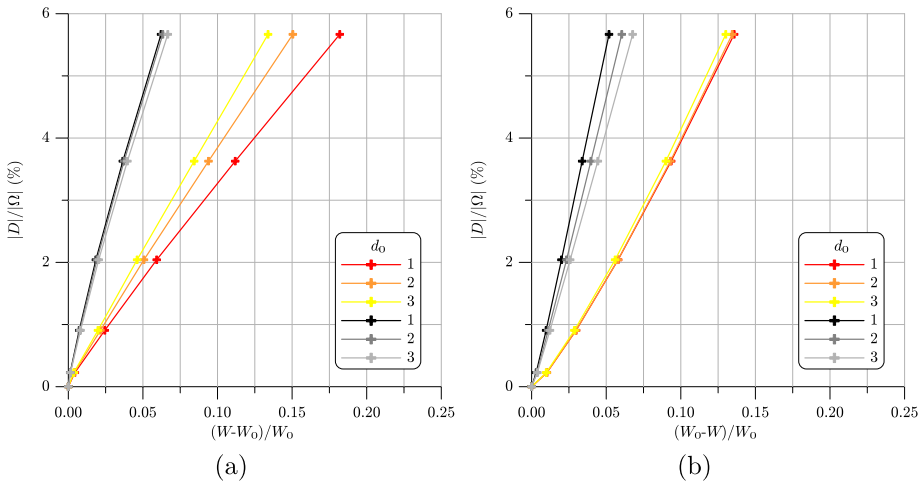
**Fig. 5** Influence of $d_0$ for square inclusions in Test $T_2$ of Fig. 3b ($21 \times 21$ FE mesh): $k = 0.1$ (**a**), $k = 10$ (**b**)
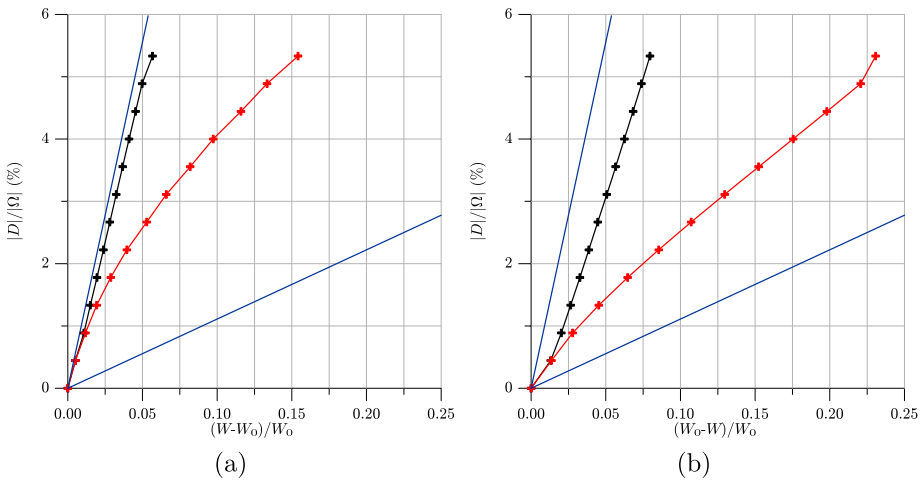


**Fig. 6** Numerical size estimates for inclusions of general shape generated from a generic element inside $\Omega$ for test $T_1$ of Fig. 3a ($21 \times 21$ FE mesh, $d_0 = 2$): $k = 0.1$ (**a**), $k = 10$ (**b**)

The straight lines drawn in Figs. 4 and 6 correspond to the theoretical size estimates for test $T_1$ of Fig. 3a. For both cases $k = 0.1$ and $k = 10$ we have

$$\frac{1}{9}\frac{|W - W_0|}{W_0} \leq \frac{|D|}{|\Omega|} \leq \frac{10}{9}\frac{|W - W_0|}{W_0}. \tag{2.11}$$

The comparison with the region of the plane $\left(\frac{|D|}{|\Omega|}, \frac{|W-W_0|}{W_0}\right)$ covered by the corresponding numerical experiments confirms, as already remarked in [19] in the context of linear elasticity, that practical applications of the size estimates approach lead to less pessimistic results with respect to those obtained via the theoretical analysis.
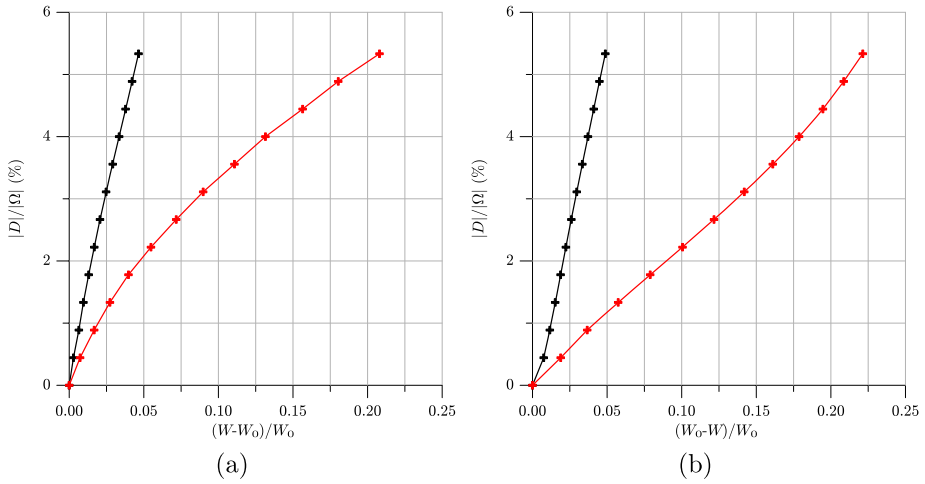
**Fig. 7** Numerical size estimates for inclusions of general shape generated from a generic element inside $\Omega$ for test $T_2$ of Fig. 3b ($21 \times 21$ FE mesh, $d_0 = 2$): $k = 0.1$ (**a**), $k = 10$ (**b**)

## 2.3 Three-Dimensional Case

The first part of this subsection is devoted to the extension to the 3-D case of the numerical simulations given in Sect. 2.2. In the second part, we shall investigate the effect of the oscillation character of the Neumann data on the upper bound of size inclusion.

Similarly to the 2-D case, a first series of numerical simulations has been performed on an electrical conductor of cubic shape, with side $l$, with the two current density fields illustrated in Fig. 8. In both cases, a mesh of $20 \times 20 \times 20$ finite elements has been considered when performing simulations in presence of cubic inclusions. The results are illustrated in Figs. 9 and 10. Figure 9 contains also the straight lines corresponding to the theoretical size estimates for test $T_1$ of Fig. 8, that is

$$\frac{1}{9} \frac{|W - W_0|}{W_0} \leq \frac{|D|}{|\Omega|} \leq \frac{10}{9} \frac{|W - W_0|}{W_0}. \tag{2.12}$$

In order to deal with inclusions of general shape, however, the numerical experiments require some restrictions to reduce the computer time. A rough estimate of the computational cost can be obtained noting that the numerical effort is essentially due to the solution of the linear system (2.9). Denoting by $m$ the number of the equations and by $b$ the half bandwidth of the matrix, the decomposition requires $m(b - 1)$ multiplications and $mb(b - 1)$ additions, whereas the computation of the solution involves $mb$ multiplications.

Therefore, for each given inclusion in a $20 \times 20 \times 20$ FE mesh, a linear system of 10648 ($b = 1015$) equations has to be solved, requiring a computer time of approximately 86 s working on an Opteron 2.4 GHz computer. Since the number of all possible inclusions formed by $n_i$ elements on a mesh of $n_e \times n_e \times n_e$ is $\frac{n_e^3!}{n_i!(n_e^3 - n_i)!}$, the treatment of all the possible cases is practically impossible. Indeed by considering that the $20 \times 20 \times 20$ is formed by 8000 elements and that, if the ratio $|D|/|\Omega|$ is less than 6% that is 480 elements, the number of cases to analyze is $69.1183 \times 10^{785}$.

In order to reduce the computer time significantly we have considered a $7 \times 7 \times 7$ mesh generating a system of 729 equations. Despite of this, the number of possible cases to con-
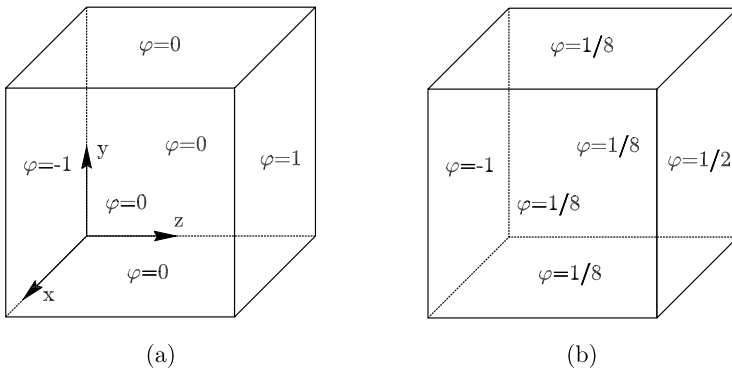
**Fig. 8** Cubic conductor considered in 3-D numerical simulations for the EIT model and applied current density fields: Test $T_1$ (**a**) and Test $T_2$ (**b**)
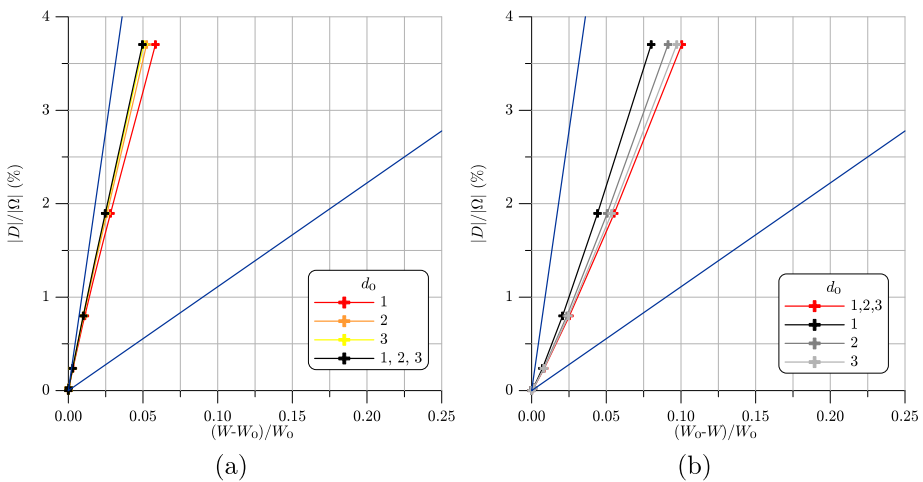


**Fig. 9** Influence of $d_0$ for cubic inclusions in test $T_1$ of Fig. 8 ($20 \times 20 \times 20$ FE mesh): $k = 0.1$ (**a**), $k = 10$ (**b**)

sider still remains very high; for instance, for inclusions formed by 5 elements, one has to solve about $3.8 \times 10^{10}$ linear systems. Therefore, we decided to restrict our analysis to inclusions satisfying the following additional conditions:

(i) The inclusion is the union of elements having at least one common face and it is formed by starting from a generic element inside an octant of the cube (this last assumption is not really restrictive due to the symmetries of the problem).

(ii) $d_0 = 1$.

For inclusions formed by $1, \dots, 7$ elements, we have considered all possible inclusions satisfying the limitations (i) and (ii), whereas for inclusions formed by $8, \dots, 17$ elements we have considered a random sample because of the high computational cost. For these cases, the ratio between the sample dimension and that of all the data approximately spans between 20% for inclusions formed by 8 elements and 0.01% for inclusions formed by 17 elements. The results are presented in Figs. 11 and 12 for Test $T_1$ and Test $T_2$, respectively. In Fig. 11,
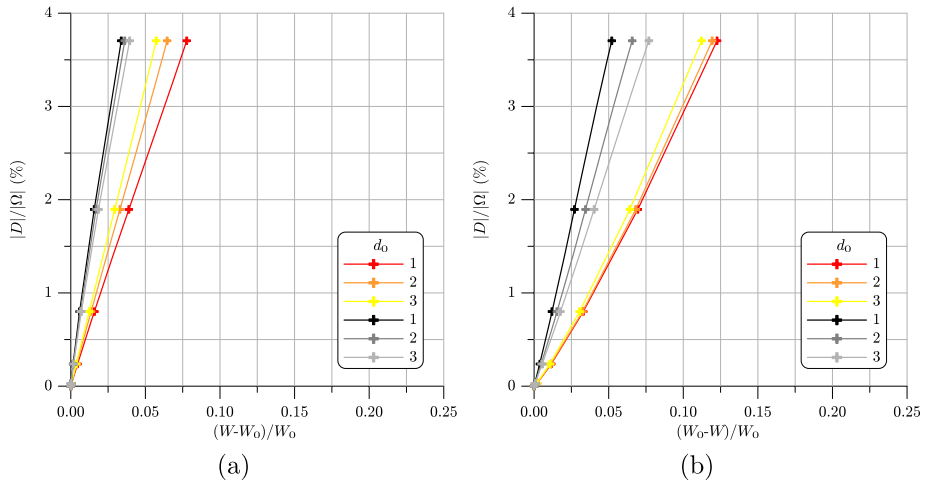
**Fig. 10** Influence of $d_0$ for cubic inclusions in test $T_2$ of Fig. 8 ($20 \times 20 \times 20$ FE mesh): $k = 0.1$ (**a**), $k = 10$ (**b**)
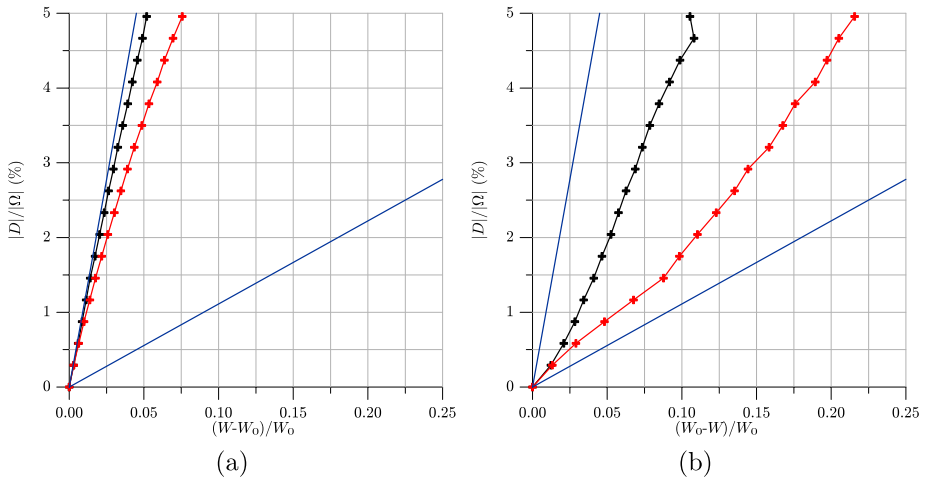


**Fig. 11** Numerical size estimates for inclusions of general shape generated from a generic element belonging to an eight of the cube for test $T_1$ of Fig. 8a ($7 \times 7 \times 7$ FE mesh, $d_0 = 1$): $k = 0.1$ (**a**), $k = 10$ (**b**)

the straight lines corresponding to the theoretical bounds (2.12) for Test $T_1$ are also drawn. As already remarked in the treatment of the 2-D case, the theoretical analysis leads to rather pessimistic results with respect to those obtained by the numerical simulations, especially when the inclusion is softer than the surrounding material.

The Neumann data considered in the above experiments give rise to potential fields inside the conductor with nonvanishing gradient. In the general case, when the gradient of the solution may vanish, we expect, accordingly to Theorems 1.1, 1.2, that the upper bounds deteriorate as the frequency $F[\varphi]$ given by (1.8) increases. Since $F[\varphi]$ is a ratio which
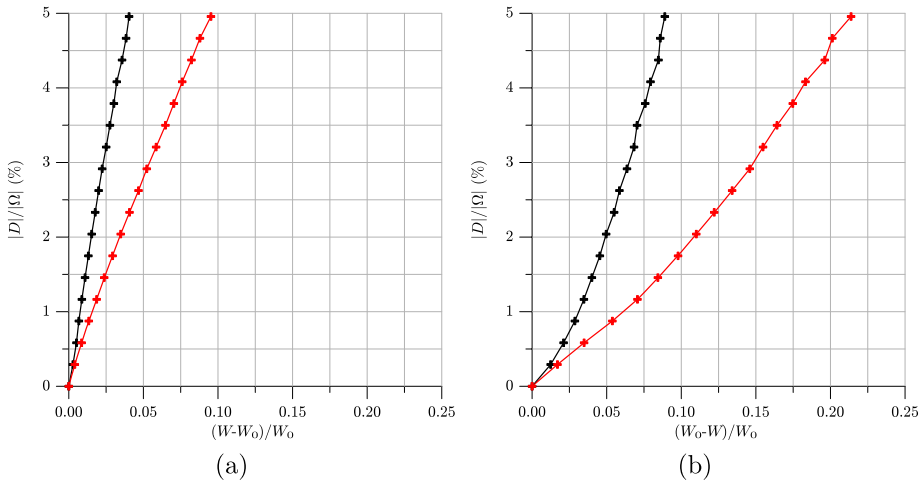
**Fig. 12** Numerical size estimates for inclusions of general shape generated from a generic element belonging to an eight of the cube for test $T_2$ of Fig. 8a ($7 \times 7 \times 7$ FE mesh, $d_0 = 1$): $k = 0.1$ (**a**), $k = 10$ (**b**)

measures the frequency of oscillation of $\varphi$, we are interested to investigate the effectiveness of the size estimates approach for oscillating Neumann data.

In particular, the numerical simulations have been carried out for the cubic electrical conductor considered before and choosing the following Neumann data:

$$\left.\begin{array}{ll} \varphi = -\cos\frac{n\pi x}{l}, & \text{on } z = 0, \\ \varphi = \cos\frac{n\pi x}{l}, & \text{on } z = l, \\ \varphi = 0, & \text{elsewhere on } \partial\Omega, \end{array}\right\} \quad \text{for } n = 0, 1, 2. \quad (2.13)$$

Case $n = 0$ has been already discussed at the beginning of this paragraph and corresponds to the simple case in which the gradient of the unperturbed solution $u_0$ does not vanish in $\Omega$.

The two other cases are examples of Neumann data with higher frequency $F[\varphi]$. More precisely, the corresponding solutions $u_0$ have critical lines of equation

$$\left\{ x = \frac{l}{n}\left(\frac{1}{2}+i\right), z = \frac{l}{n}\left(\frac{1}{2}+j\right) \right\}, \quad i, j = 0, \dots, n - 1.$$

The mesh employed consists of $20 \times 20 \times 20$ HC finite elements. The analysis has been focussed on cubic inclusions having volume up to 6% of the total volume of the specimen and conductivity $k = 0.1$ and $k = 10$. The numerical results for $n = 1$ and $n = 2$ are presented in Figs. 13 and 14, respectively. The numerical results show that the lower bound for size estimates (1.10), (1.11) improves as $d_0$ increases, whereas the upper bound of $|D|$ is rather insensitive to the choice of $d_0$.
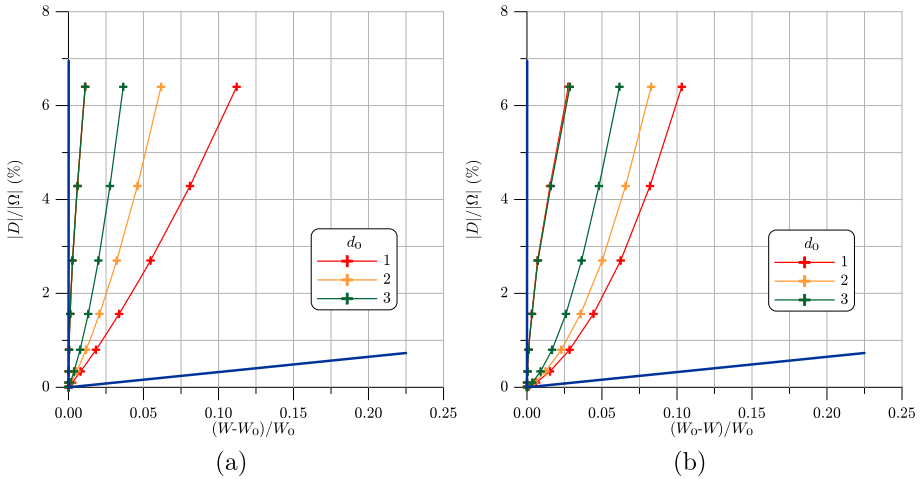
**Fig. 13** Cubic electrical conductor with Neumann data as in case $n = 1$ of (2.13): lower and upper bound of the power gap for different values of $d_0$ ($k = 0.1$ (**a**) and $k = 10$ (**b**)) on a $20 \times 20 \times 20$ mesh

Theoretical estimates for cases $n = 1$ and $n = 2$ of (2.13) are given by

for $k > 1$:

$$\frac{\tanh \frac{n\pi}{2}}{n\pi(k-1)} \frac{W_0 - W}{W_0} \leq \frac{|D|}{|\Omega|} \leq \frac{1}{C_n} \frac{k}{k-1} \frac{\tanh \frac{n\pi}{2}}{n\pi} \frac{W_0 - W}{W_0};$$

for $k < 1$:

$$\frac{k}{n\pi(1-k)} \tanh \frac{n\pi}{2} \frac{W - W_0}{W_0} \leq \frac{|D|}{|\Omega|} \leq \frac{1}{C_n} \frac{1}{1-k} \frac{\tanh \frac{n\pi}{2}}{n\pi} \frac{W - W_0}{W_0},$$

(2.14)

where

$$C_n = \frac{10}{n\pi \cosh^2 \frac{n\pi}{2}} \left( \sinh \frac{n\pi}{20} - \sin \frac{n\pi}{20} \right), \quad n = 1, 2.$$

The theoretical estimates are indicated in Figs. 13 and 14. The slope of the straight line corresponding to the upper bound is so high that it practically coincides with the vertical axis, at least for the portion of graph near the origin considered in this study. The theoretical lower bound gives, for a fixed power gap, values significantly smaller than those obtained in the numerical experiments.

## 3 Numerical Simulations for the Complete EIT Model

### 3.1 Numerical Model

In this case, by using the same notation introduced in Sect. 2, the energy functional $J : H^1(\Omega) \times \mathbb{R}^L \to \mathbb{R}$ related to the variational formulation of problem (1.13) is given by

$$J(u, U^l) = \frac{1}{2} \int_\Omega (1 + (k-1)\chi_D) \nabla u \cdot \nabla u + \frac{1}{2} \sum_{l=1}^L \frac{1}{z_l} \int_{\partial \Omega_l} (u - U^l)^2 - \sum_{l=1}^L I_l U^l. \quad (3.1)$$
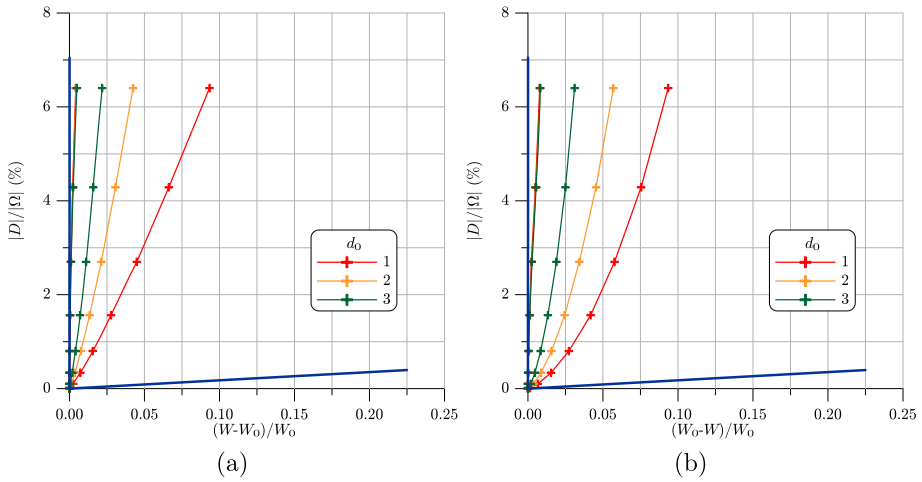
**Fig. 14** Cubic electrical conductor with Neumann data as in case $n = 2$ of (2.13): lower and upper bound of the power gap for different values of $d_0$ ($k = 0.1$ (**a**) and $k = 10$ (**b**)) on a $20 \times 20 \times 20$ mesh

Using HC interpolation for the potential field $u$ and with the notation introduced in Sect. 2, the discrete energy functional becomes

$$J(\mathbf{w}_e, U^l) = \frac{1}{2} \sum_e \int_{\Omega_e} (1 + (k-1)\chi_D)(\nabla \mathbf{N}_e \mathbf{w}_e) \cdot (\nabla \mathbf{N}_e \mathbf{w}_e)$$

$$+ \frac{1}{2} \sum_{l=1}^{L} \frac{1}{z_l} \sum_{\hat{e}} \int_{(\partial \Omega_l)_e} (\mathbf{N}_e \mathbf{w}_e - U^l)^2 - \sum_{l=1}^{L} I_l U^l, \tag{3.2}$$

or

$$J(\mathbf{w}_e, U^l) = \frac{1}{2} \sum_e \mathbf{w}_e^T \mathbf{K}_e \mathbf{w}_e$$

$$+ \frac{1}{2} \sum_{l=1}^{L} \frac{1}{z_l} \sum_{\hat{e}} (\mathbf{w}_e^T \mathbf{K}_{ll} \mathbf{w}_e + (U^l)^2 - 2\mathbf{w}_e^T \mathbf{K}_{el} U^l) - \sum_{l=1}^{L} I_l U^l, \tag{3.3}$$

having used the compact notation

$$\mathbf{K}_e = \int_{\Omega_e} (1 + (k-1)\chi_D)(\nabla \mathbf{N}_e)^T \nabla \mathbf{N}_e,$$

$$\mathbf{K}_{ll} = \int_{(\partial \Omega_l)_e} \mathbf{N}_e^T \mathbf{N}_e, \tag{3.4}$$

$$\mathbf{K}_{el} = \int_{(\partial \Omega_l)_e} \mathbf{N}_e^T.$$

We remark that the second sum in the right hand side of (3.2) and (3.3), that on $\hat{e}$, is extended only to the elements under the electrodes.
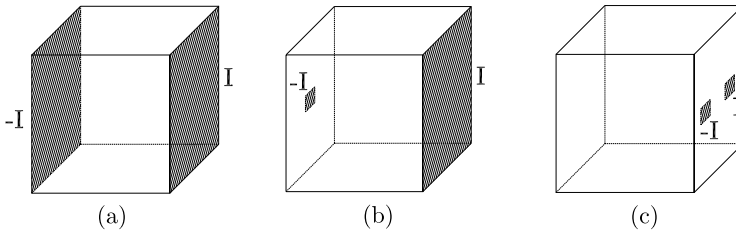
**Fig. 15** Cubic conductor considered in 3-D numerical simulations for the physical EIT model and location of the electrodes: test $T_1$ (**a**), test $T_2$ (**b**) and test $T_3$ (**c**)

Collecting the unknown parameters representing the potential field in **w**, those of the electrodes in **U** and the current pattern in **I**, by a standard method of assembling we obtain the following linear system

$$\begin{bmatrix} \mathbf{K}_{ww} & -\mathbf{K}_{wU} \\ -\mathbf{K}_{wU}^T & \mathbf{K}_{UU} \end{bmatrix} \begin{bmatrix} \mathbf{w} \\ \mathbf{U} \end{bmatrix} = \begin{bmatrix} \mathbf{0} \\ \mathbf{I} \end{bmatrix}, \tag{3.5}$$

which can be efficiently solved through a two–step scheme: in the first step the vector **w** is computed exploiting the diagonal form of the matrix $\mathbf{K}_{UU}$; in the second step **U** is evaluated on the basis of **w**.

## 3.2 Results for 3-D Cases

The analysis has been restricted to the case of two electrodes located on the boundary of a cubic electrical conductor of side $l$, see Fig. 15. The specimen has been discretized by a mesh of $17 \times 17 \times 17$ cubic HC finite elements and the numerical experiments have been carried out on cubic inclusions only, with volume up to 6% of the total volume and conductivity value $k = 0.1$ or $k = 10$. The surface impedance takes a constant value such that $\zeta = \frac{z\sigma}{l} = 0.2$ on both electrodes, according to properties of human skin reported in literature, see, for instance [26].

In test $T_1$ of Fig. 15, the electrodes cover completely two opposite faces of the specimen, whereas in Test $T_2$ one electrode coincides with a face of $\partial\Omega$ and the other is a square, formed by one or nine surface finite elements, and it is located in central position of the opposite face. Finally, in Test $T_3$, two electrodes are placed on the same face of the conductor $\Omega$ in a symmetric way with respect to middle lines of the face. The electrodes are separated by three finite elements and their dimensions are equal to the element size.

The numerical results for Test $T_1$ are presented in Fig. 16 for $k = 0.1$ and $k = 10$, respectively, and for varying values of $d_0$. For both cases $k = 0.1$ and $k = 10$, the theoretical size estimates are given by

$$\frac{1}{9}\left(\frac{l+2z}{l}\right)\frac{|W - W_0|}{W_0} \leq \frac{|D|}{|\Omega|} \leq \frac{10}{9}\left(\frac{l+2z}{l}\right)\frac{|W - W_0|}{W_0}$$

and, again, they lead to a rather pessimistic evaluation of the upper and lower bounds.

Concerning Test $T_2$, Fig. 17 shows the results when the small electrode coincides with one surface finite element, whereas Fig. 18 refers to the case of a $3 \times 3$ finite elements electrode. One can notice that in all the four cases, the upper bound is not really influenced by the value of $d_0$. Moreover, the inaccuracy in determining the lower bound of the angular
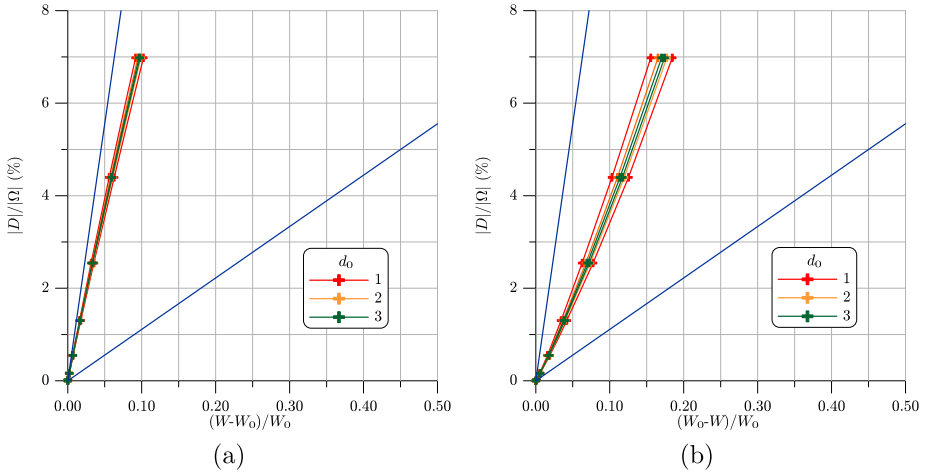
**Fig. 16** Influence of $d_0$ for cubic inclusions in Test $T_1$ of Fig. 15a ($17 \times 17 \times 17$ FE mesh, $\zeta = 0.2$): $k = 0.1$ (**a**), $k = 10$ (**b**)
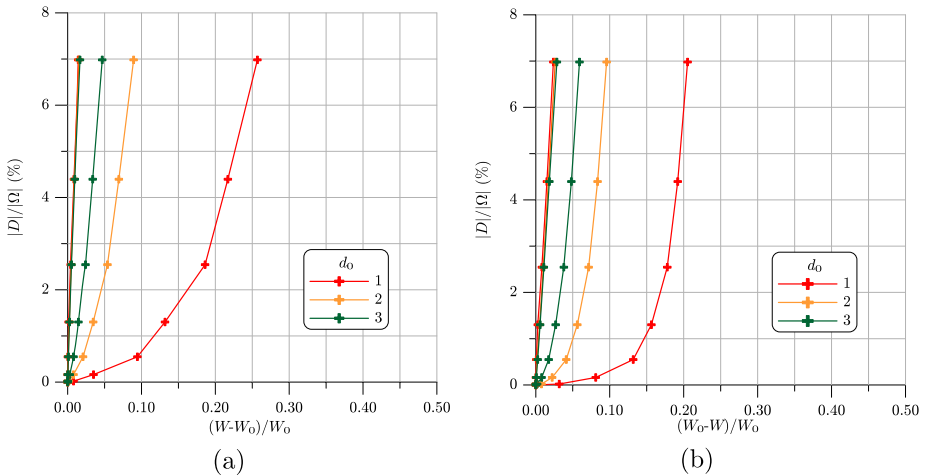


**Fig. 17** Influence of $d_0$ for cubic inclusions in Test $T_2$ of Fig. 15b ($17 \times 17 \times 17$ FE mesh, $\zeta = 0.2$, $1 \times 1$ FE electrode): $k = 0.1$ (**a**), $k = 10$ (**b**)

sector, is probably due to the fact that the present analysis is restricted to the special class of cubic inclusions.

A comparison between Fig. 17 and Fig. 18 suggests that better upper bounds can be obtained by enlarging the size of the small electrode. Moreover, from Figs. 17 and 18 it appears clearly that the lower bound significantly improves as the distance $d_0$ between the inclusion $D$ and the boundary of $\Omega$ increases. This property has been further investigated by increasing only the distance $d_{03}$ of the inclusion $D$ from the face of the conductor containing the small electrode. Figure 19 shows the results of simulations in the case of a single finite element electrode and a comparison with Fig. 17 suggests that the improvement of the lower bound is mainly due to the greater distance from the electrode.
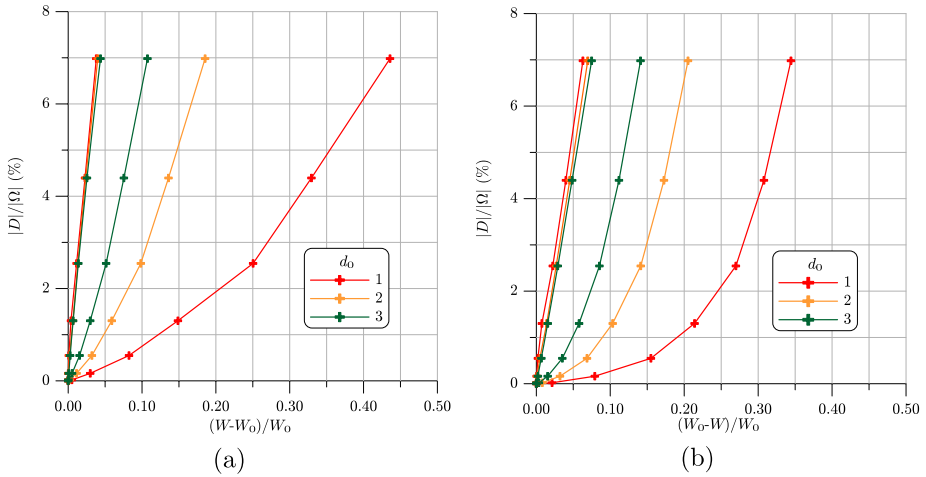
**Fig. 18** Influence of $d_0$ for cubic inclusions in Test $T_2$ of Fig. 15b ($17 \times 17 \times 17$ FE mesh, $\zeta = 0.2$, $3 \times 3$ FE electrode): $k = 0.1$ (**a**), $k = 10$ (**b**)
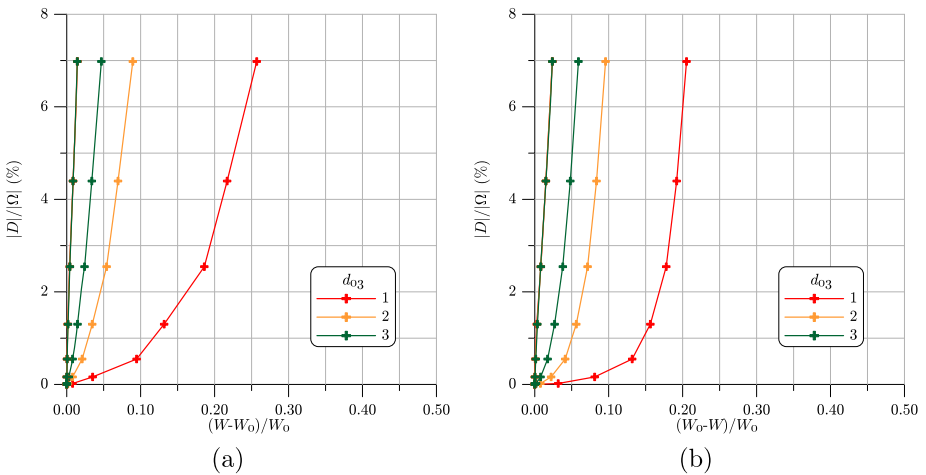


**Fig. 19** Influence of $d_{03}$ for cubic inclusions in Test $T_2$ of Fig. 15b ($17 \times 17 \times 17$ FE mesh, $\zeta = 0.2$, $1 \times 1$ FE electrode): $k = 0.1$ (**a**), $k = 10$ (**b**)

Finally, the results of the numerical simulations for Test $T_3$ are presented in Fig. 20. In this case, the lower bound improves as the distance $d_0$ between the inclusion $D$ and the boundary of $\Omega$ increases, whereas the upper bound is indistinguishable from the vertical axis.

## 4 Conclusions

We have tested by numerical simulations the approach of *size estimates* for EIT. We could perform experiments in the 2-D setting with a large varieties of shapes of inclusions and we
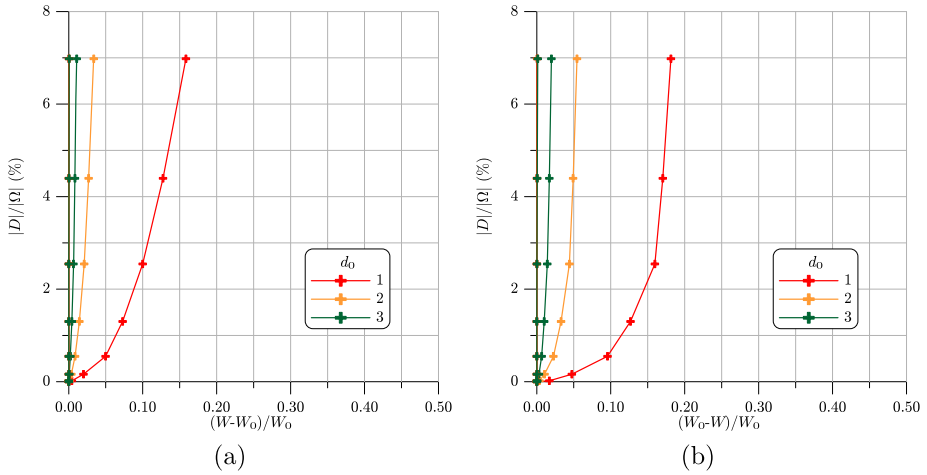
**Fig. 20** Influence of $d_0$ for cubic inclusions in Test $T_3$ of Fig. 15c ($17 \times 17 \times 17$ FE mesh, $\zeta = 0.2$, $1 \times 1$ FE electrode): $k = 0.1$ (**a**), $k = 10$ (**b**)

found quite satisfactory bounds, which in some cases are markedly better than those derived theoretically.

In the 3-D case, we had to limit the variety of shapes of the test inclusions since the growth of their degree of freedom conflicts with the limitations of computer time. We showed that good volume bounds hold when the boundary data $\varphi$ is *well-behaved* in terms of its frequency, whereas they rapidly deteriorate as the frequency increases.

For the complete EIT model we have also made tests in a 3-D setting and compared the bounds in terms of the size of the electrodes, their relative distance and their a priori assumed distance from the inclusion $D$. We have shown that we obtain good bounds when the electrodes are not too small and when $D$ is sufficiently distant from them.

## References

1. Alessandrini, G.: Stable determination of conductivity by boundary measurements. Appl. Anal. **27**, 153–172 (1988)
2. Mandache, N.: Exponential instability in an inverse problem for the Schrödinger equation. Inverse Probl. **17**, 1435–1444 (2001)
3. Alessandrini, G., Vessella, S.: Lipschitz stability for the inverse conductivity problem. Adv. Appl. Math. **35**, 207–241 (2005)
4. Friedman, A.: Detection of mines by electric measurements. SIAM J. Appl. Math. **47**, 201–212 (1987)
5. Friedman, A., Gustafsson, B.: Identification of the conductivity coefficient in an elliptic equation. SIAM J. Math. Anal. **18**, 777–787 (1987)
6. Friedman, A., Isakov, V.: On the uniqueness in the inverse conductivity problem with one measurement. Indiana Univ. Math. J. **38**, 563–579 (1989)
7. Alessandrini, G., Isakov, V.: Analyticity and uniqueness for the inverse conductivity problem. Rend. Ist. Mat. Univ. Trieste **28**, 351–370 (1996)
8. Fabes, E., Kang, H., Seo, J.K.: Inverse conductivity problem with one measurement: error estimates and approximate identification for perturbed disks. SIAM J. Math. Anal. **30**, 699–720 (1999)

9. Alessandrini, G., Isakov, V., Powell, J.: Local uniqueness in the inverse conductivity problem with one measurement. Trans. Am. Math. Soc. **347**, 3031–3041 (1995)
10. Isakov, V.: On uniqueness of recovery of a discontinuous conductivity coefficient. Commun. Pure Appl. Math. **41**, 865–877 (1988)
11. Isakov, V.: Inverse Problems for Partial Differential Equations. Springer, New York (1998)
12. Di Cristo, M., Rondi, L.: Examples of exponential instability for inverse inclusion and scattering problems. Inverse Probl. **19**, 685–701 (2003)
13. Alessandrini, G., Rosset, E.: The inverse conductivity problem with one measurement: bounds on the size of the unknown object. SIAM J. Appl. Math. **58**, 1060–1071 (1998)
14. Kang, H., Seo, J.K., Sheen, D.: The inverse conductivity problem with one measurement: stability and estimation of size. SIAM J. Math. Anal. **28**, 1389–1405 (1997)
15. Alessandrini, G., Rosset, E., Seo, J.K.: Optimal size estimates for the inverse conductivity problem with one measurement. Proc. Am. Math. Soc. **128**, 53–64 (2000)
16. Alessandrini, G., Morassi, A., Rosset, E.: Size estimates. In: Alessandrini, G., Uhlmann, G. (eds.) Inverse Problems: Theory and Applications. Contemp. Math., vol. 333, pp. 1–33. American Mathematical Society, Providence (2003)
17. Ikehata, M.: Size estimation of inclusion. J. Inverse Ill-Posed Probl. **6**, 127–140 (1998)
18. Alessandrini, G., Morassi, A., Rosset, E.: Detecting an inclusion in an elastic body by boundary measurements. SIAM Rev. **46**, 477–498 (2004). Revised and updated version of SIAM J. Math. Anal. **3**, 1247–1268 (2002)
19. Alessandrini, G., Bilotta, A., Formica, G., Morassi, A., Rosset, E., Turco, E.: Numerical size estimates of inclusions in elastic bodies. Inverse Probl. **21**, 133–151 (2005)
20. Cheng, K.S., Isaacson, D., Newell, J.C., Gisser, D.G.: Electrode models for electric current computed tomography. IEEE Trans. Biomed. Eng. **36**, 918–924 (1989)
21. Paulson, K., Breckon, W., Pidcock, M.: Electrode modelling in electrical impedance tomography. SIAM J. Appl. Math. **52**, 1012–1022 (1992)
22. Somersalo, E., Cheney, M., Isaacson, D.: Existence and uniqueness for the electrode models for electric current computed tomography. SIAM J. Appl. Math. **52**, 1023–1040 (1992)
23. Alessandrini, G., Rosset, E.: Volume bounds of inclusions from physical EIT measurements. Inverse Probl. **20**, 575–588 (2004)
24. Aristodemo, M.: A high-continuity finite element model for two-dimensional elastic problems. Comput. Struct. **21**, 987–993 (1985)
25. Bilotta, A., Formica, G., Turco, E.: Performances of a high-continuity finite element in three-dimensional elasticity. Report LabMeC No. 26, www.labmec.unical.it, 2003; submitted to Computer and Structures
26. Surowiec, A.J., Stuchly, S.S., Barr, J.R., Swarup, A.: Dielectric properties of breast carcinoma and the surrounding tissues. IEEE Trans. Biomed. Eng. **35**, 257–263 (1988)